

Journal of Materials Chemistry A

Materials for energy and sustainability

Accepted Manuscript

This article can be cited before page numbers have been issued, to do this please use: C. Tewari, K. S. Rawat, D. Bhatt, B. Santhibhushan, Y. N. Kim, S. Yoon, A. Srivastava, J. Zha, N. G. Sahoo and Y. C. Jung, *J. Mater. Chem. A*, 2026, DOI: 10.1039/D6TA01141A.



This is an Accepted Manuscript, which has been through the Royal Society of Chemistry peer review process and has been accepted for publication.

Accepted Manuscripts are published online shortly after acceptance, before technical editing, formatting and proof reading. Using this free service, authors can make their results available to the community, in citable form, before we publish the edited article. We will replace this Accepted Manuscript with the edited and formatted Advance Article as soon as it is available.

You can find more information about Accepted Manuscripts in the [Information for Authors](#).

Please note that technical editing may introduce minor changes to the text and/or graphics, which may alter content. The journal's standard [Terms & Conditions](#) and the [Ethical guidelines](#) still apply. In no event shall the Royal Society of Chemistry be held responsible for any errors or omissions in this Accepted Manuscript or any consequences arising from the use of any information it contains.

Biomass-Derived Potassium-Doped Reduced Graphene Oxide-like Material for High-Performance Supercapacitors: Experimental and Computational Analysis

Chetna Tewari^a, Kundan Singh Rawat^{a,b}, Diksha Bhatt^b, Boddepalli SanthiBhushan^c, Young Nam Kim^a, Somi Yoon^{a,d}, Anurag Srivastava^e, Jun-Wei Zha^f, Nanda Gopal Sahoo^c, Yong Chae Jung^{a,*}

^a RAMP Convergence Research Center, Korea Institute of Science and Technology (KIST), 92 Chudong-ro, Bongdong-eup, Wanju-gun, Jeonbuk, 55324, Republic of Korea.

^b Prof. Rajendra Singh Nanoscience and Nanotechnology Centre, Department of Chemistry D.S.B. Campus, Kumaun University Nainital, Uttarakhand, India.

^c Department of Electronics and Communications Engineering, Indian Institute of Information Technology, Allahabad, UP-211015

^d Department of Organic and Nano Engineering, Hanyang University, 222 Wangsimni-ro, Seongdong-gu, Seoul 04763, Republic of Korea

^e Department of Engineering Sciences, ABV – Indian Institute of Information Technology and Management, Gwalior, M.P. – 474015

^f State Key Laboratory of Alternate Electrical Power System with Renewable Energy Sources, School of Electrical and Electronic Engineering, North China Electric Power University, Beijing 102206, China

* Corresponding authors emails: ycjung@kist.re.kr (Yong Chae Jung)

ABSTRACT

With the growing energy demand and limited resources, the development of cost-effective and efficient materials is essential. Among these, carbon-based nanomaterials offer promising characteristics for energy applications. Bio-based carbon nanomaterials are particularly promising for energy storage devices like supercapacitors due to their sustainability and performance characteristics. This study presents a cost-effective method for synthesizing bio-based reduced graphene oxide (rGO)-like material using persimmon fruit, a readily available resource in east Asia. A clean two-step thermal process was employed to synthesize rGO-like material, eliminating the need for toxic chemicals commonly used in conventional approaches. The material is derived from persimmon and naturally doped with potassium, which contributes to enhanced



1 supercapacitor performance. A systematic optimization of carbonization temperature
2 (600–1000 °C) and heating rate (5–15 °C min⁻¹) was carried out using residual yield
3 analysis, Raman spectroscopy, XRD, and TGA, identifying 800 °C and 10 °C min⁻¹ as
4 the optimal synthesis conditions. Density Functional Theory (DFT) calculations were
5 performed to elucidate the electronic structure and validate the improved
6 electrochemical properties observed experimentally. The electrochemical performance
7 of the synthesized material, was investigated in acidic, basic, and neutral electrolytes,
8 using a three-electrode setup. The maximum Cs achieved was 302 F/g at a scan rate of
9 2 mV/s was achieved in acidic electrolyte. Furthermore, a symmetric supercapacitor
10 device fabricated using the synthesized material demonstrated a specific capacitance of
11 98 F/g, an energy density of 11 Wh/kg, and a power density of 89.8 W/kg at a current
12 density of 0.2 A/g. Remarkably, the device maintained its original capacitance even
13 after 5000 charge-discharge cycles. These results highlight the potential of potassium-
14 doped, biomass-derived rGO-like materials as effective electrode materials for
15 supercapacitor applications.

16
17 **Keywords:** Bio-material, Energy storage, Reduced graphene oxide, Supercapacitor.

18 19 1. Introduction

20 Research into energy storage devices has gained significant momentum due to the
21 increasing demand for high-performance electronics and renewable energy sources.^{1,2}
22 Supercapacitors (SCs) have emerged as promising candidates for energy storage due to
23 their extended cycle life, high power density, and rapid charge-discharge rates.^{3,4} The
24 performance of SCs is heavily influenced by electrode materials, with carbon-based
25 nanomaterials such as zero-dimensional carbon spheres, one-dimensional carbon
26 nanotubes, two-dimensional graphene, and three-dimensional hydrogels/aerogels being
27 extensively studied.⁵⁻⁷ Among these, graphene stands out for its exceptional properties
28 including high surface area, porosity, two-dimensional structure, and excellent
29 electrical conductivity.⁸

30 Research has shown that introducing metallic and non-metallic elements alters surface
31 properties and enhances conductivity.⁹ For instance, Morengi et al. demonstrated a
32 graphene electrode coated with nickel nanoparticles achieving specific energy and



1 power densities of 37 Wh/kg and 5 kW/kg, respectively.¹⁰ Heteroatom doping
2 techniques such as solution-based doping, gas-phase doping, and others have been
3 employed to enhance electronic properties and tailor surface chemistry, although
4 natural metal doping remains less explored.

5 While graphene-based materials exhibit superior electrochemical performance, their
6 high cost, complex manufacturing processes, and environmental impact pose
7 challenges.⁶ Recent studies have shifted toward developing scalable and cost-effective
8 synthesis methods for graphene-like materials, with a focus on structural design and
9 electrochemical optimization. Biomass, being rich in carbohydrates, fibers, and
10 minerals, is considered a sustainable and versatile precursor for carbon-based
11 materials.^{11,12} Biomass-derived graphene-based materials have garnered attention for
12 their affordability, renewability, and eco-friendliness.³ For instance, Cao et al.
13 developed lignin-based aerogels with organized structures achieving an energy density
14 of 32 Wh/kg,¹³ and Wang et al. synthesized cellulose nanofiber/multi-walled carbon
15 nanotube composites with a specific capacitance of 114.8 F/g.¹⁴ Akhavan et al. used a
16 modified Hummers' method to synthesize reduced graphene oxide (rGO) from various
17 industrial carbonaceous wastes, including fruit and agricultural residues.¹⁵ Similarly,
18 large-scale production of graphene-based materials has been reported from waste
19 tires,¹⁶ plastics,¹⁷⁻¹⁹ and agricultural biomass²⁰⁻²² for supercapacitor applications.
20 However, reports on the synthesis of graphene-like materials from biomass naturally
21 doped with functional metallic elements are still limited.

22 In particular, potassium doping has emerged as a promising strategy for enhancing the
23 electrochemical performance of supercapacitor electrodes. Potassium incorporation is
24 known to increase electrical conductivity and facilitate fast ion
25 intercalation/deintercalation, resulting in improved specific capacitance and rate
26 capability. For example, potassium-doped Sr–Cu metal oxide (K-SrCu₂O₂) showed a
27 much higher capacitance of 438 F/g at 1 A/g, compared to just 14.5 F/g for the undoped
28 material, due to their better charge movement and activated tunnel-like structures.²³
29 Additionally, potassium-assisted biomass carbonization contributes to the formation of
30 highly porous architectures with abundant active sites, further enhancing capacitance.²⁴
31 K-doping in electrolytes also improves ionic conductivity and expands the
32 electrochemical window, enabling higher energy and power densities.²⁵ These findings

View Article Online
DOI: 10.1039/D6TA01141A



1 collectively underscore potassium's multifaceted role in boosting both electrode and
2 electrolyte performance, making it a valuable dopant in supercapacitor design.

3 In this context, producing rGO-like materials from unconventional, mineral-rich
4 biomass sources such as persimmon fruit is of growing interest. The Hachiya variety of
5 persimmon, heart- or acorn-shaped and native to east Asia, is rich in soluble tannins
6 and essential minerals including potassium, phosphorus, calcium, magnesium, and
7 zinc.²⁶⁻²⁷ Prior studies have shown that doping with elements such as magnesium,
8 potassium, and phosphorus significantly improves supercapacitor performance.^{24,28,29} To
9 further highlight the electrochemical potential of biomass-derived carbon materials, a
10 comparative analysis of previously reported carbon-based electrodes is presented in
11 Table S1. This comparison demonstrates that the PrGO synthesized in this study—
12 without the use of any chemical activation agents or catalysts—exhibits a competitive
13 specific capacitance relative to other doped and activated materials, highlighting its
14 potential for energy storage applications.

15 This study focuses on synthesizing rGO-like carbon materials from Hachiya persimmon
16 fruit through a two-step thermal process. The resulting material is naturally doped with
17 potassium, which is the most abundant metal in persimmon compared to other elements.

18 Persimmon fruit is characterized by a high moisture content (~80.9%) and a tannin
19 content of approximately 3-4%.^{27,30-31} The elemental analysis (per 100 g of persimmon
20 fruit) reveals a significantly higher potassium content (203 ± 24.10 mg) compared to
21 other elements, which are present in relatively low concentrations, such as phosphorus
22 (27 ± 2.66 mg), calcium (16 ± 4.33 mg), magnesium (11 ± 1.80 mg), sodium (10 ± 0.80
23 mg), iron (0.27 ± 0.08 mg), manganese (0.25 ± 0.04 mg), copper (0.11 ± 0.03 mg), and
24 zinc (0.10 ± 0.02 mg).²⁷ In addition, the total soluble solids, pH, protein, vitamin C, and
25 soluble tannin contents of cv. Hachiya are reported as 17.10%, 5.40, 600 mg/100 g, 12
26 mg/100 g, and 3.15 mg/100 g, respectively.²⁷

27 Consistent with this composition, our results indicate that after pyrolysis, potassium
28 remains present in significant amounts, whereas other metallic elements are retained
29 only at negligible levels. Furthermore, the relatively high potassium content (~2.15 at%)
30 suggests its important role in influencing the structural, electrical, and ion-transport
31 properties of the synthesized rGO. The electrochemical performance of the material
32 was first evaluated in a three-electrode setup using acidic, alkaline, and neutral



1 electrolytes, and the optimized electrolyte (1 M H₂SO₄) was used to evaluate the
2 supercapacitor performance in a two-electrode configuration. Additionally, Density
3 Functional Theory (DFT) analysis is conducted to elucidate the electronic structure and
4 confirm the role of potassium in enhancing charge storage behaviour. This work
5 contributes to the development of cost-effective, and high-performance electrode
6 materials for next-generation supercapacitors.

8 2. Materials and Methods

9 2.1. Materials

10 Persimmon fruit was gathered from local market of Jeonju, South Korea.
11 Excelsior provided the H₃PO₄, while Sigma Aldrich supplied the poly-vinylidene
12 fluoride (PVDF) polymer and H₂SO₄. We used every single chemical exactly as it was
13 provided to us. The graphite sheets utilized as the current collector were supplied by
14 the Madras Asbestos business. Every experiment relied on using double-distilled water.

15 2.2. Synthesis of persimmon derived-reduced graphene oxide like material

16 The persimmon-based nanomaterial has been developed by easy and cost-
17 effective two step thermal treatment as presented in Fig. S1 (ESI†, Fig. S1). In brief,
18 fresh persimmon fruit was taken and placed inside the zipper and crushed with the help
19 of roller to collect the pulp (without the outer cover and seeds). then the material
20 allowed to centrifuge at 9000 rpm to collect the fibre part. Further, 75 g material was
21 weight and low temperature carbonization has been done in Teflon hydrothermal
22 reactor with 100 mL capacity inside the oven at 180 °C temperature for 24 h. After this
23 let the reactor cooled and come in room temperature and then the resultant brown
24 coloured cylindrical sponge with weight 65.36 g was collected (some liquid material
25 also obtained). This first stage low temperature thermal treatment leads the
26 carbonization or polymerisation of the tannins present in the fruit and facilitate the
27 formation of brown coloured hydrogel with sponge texture and porous nature.
28 Subsequently, the hydrogel was freeze-dried overnight at -40 °C under vacuum
29 condition of 20 Pa. The dry weight of the resulting material was 7.66 g, indicating that
30 approximately 88% of the original mass corresponded to water/moisture content, which



1 is consistent with previously reported data.²⁷ The obtained brown cylindrical sponge
2 exhibited a height of 5.7 cm and a diameter of 3.5 cm and was characterized by its low
3 density and porous nature.

4 In the second stage, the freeze-dried hydrogel was subjected to high-
5 temperature thermal treatment in a tubular furnace under a continuous nitrogen
6 atmosphere to induce thermal reduction and structural ordering. To establish optimal
7 synthesis conditions, the carbonization temperature was systematically varied between
8 600 and 1000 °C, followed by an evaluation of the heating rate in the range of 5–15 °C
9 min⁻¹. Based on the combined analysis of residual yield, Raman spectroscopy, XRD,
10 and TGA, a carbonization temperature of 800 °C and a heating rate of 10 °C min⁻¹ were
11 identified as optimal. Under these conditions, the material was thermally treated, held
12 at the target temperature for 60 min, and subsequently cooled to room temperature at a
13 controlled rate of 2 °C/min. The resulting conductive carbon material was denoted as
14 PrGO (persimmon-derived potassium-doped reduced graphene oxide-like material).

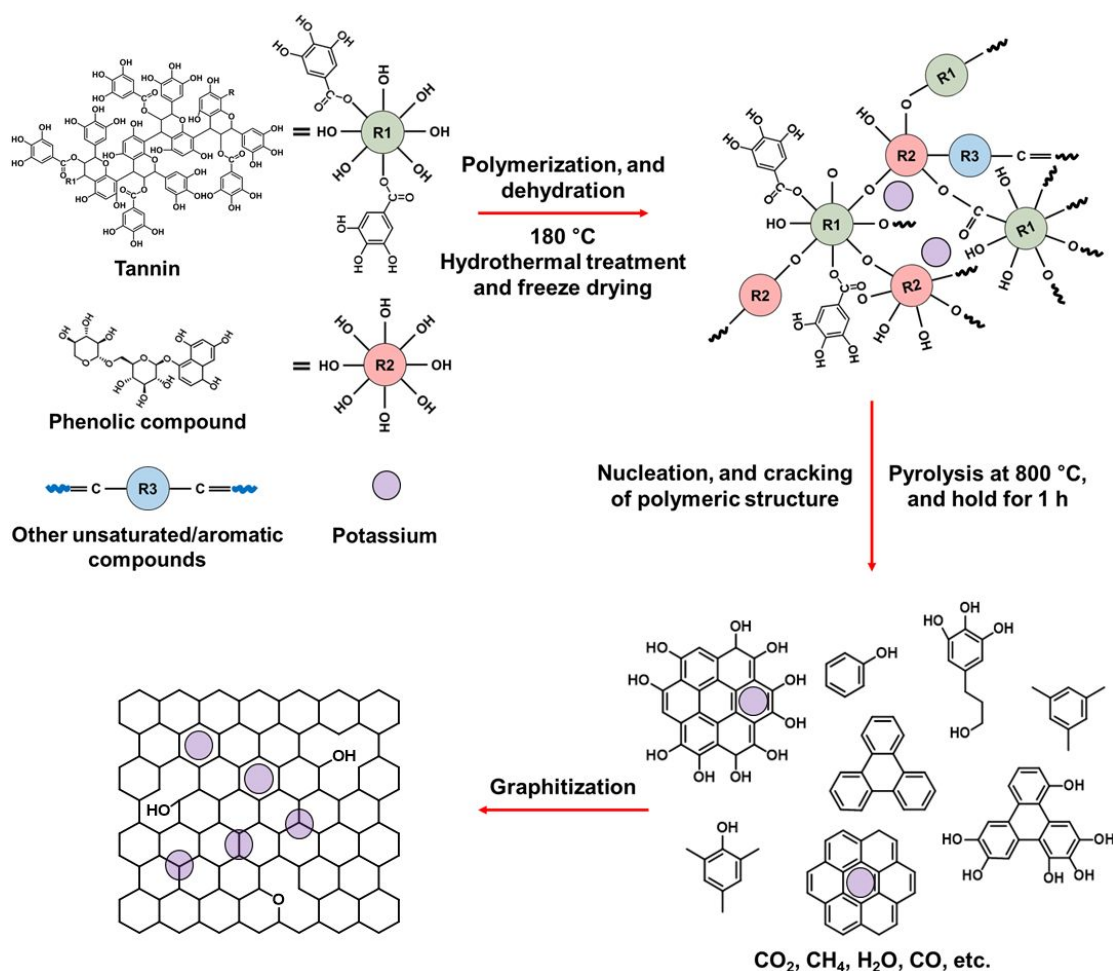
15 2.3. Schematic illustration of the formation of persimmon derived-reduced graphene 16 oxide like material

17 The synthesis of PrGO was carried out through a two-step thermal process. In the first
18 step, the fruit undergoes hydrothermal carbonization at a relatively low temperature
19 (180 °C). During this process, macromolecules such as tannins, phenolic compounds,
20 and other unsaturated/aromatic species present in persimmon undergo polymerization,
21 molecular rearrangement, and crosslinking reactions.³² These transformations result in
22 the formation of a hydrogel-like carbon framework enriched with surface functional
23 groups and containing early-stage graphitic domains. The subsequent freeze-drying step
24 promotes dehydration and preserves the porous, swollen morphology of the
25 intermediate structure.

26 In the second step, the hydrogel is subjected to high-temperature pyrolysis at 800 °C
27 under inert atmosphere. During this stage, thermal decomposition initiates nucleation
28 and the growth of small, ordered carbon clusters and aromatic domains. These domains
29 further rearrange and undergo repolymerization to form graphene-like structures,
30 accompanied by the elimination of volatile species such as CH₄, CO, and CO₂. Notably,
31 the naturally abundant potassium content in persimmon may serve as both a chemical



1 activator and dopant, promoting carbon etching, interlayer expansion, defect formation,
 2 and enhancement of electrical conductivity. The resulting carbon material exhibits a
 3 layered architecture resembling that of reduced graphene oxide. The plausible
 4 mechanism is illustrated in **Scheme 1**.



5
 6 **Scheme 1.** Illustration of the plausible mechanism for the formation of potassium
 7 doped PrGO.

8

9 3. Characterizations

10 3.1. Structural and surface characterization

11 X-ray diffraction (XRD) patterns were recorded using a Rigaku SmartLab
 12 diffractometer (9 kW) with a Cu K α radiation source ($\lambda = 1.54 \text{ \AA}$) to determine the
 13 crystalline or amorphous nature of the samples. Surface morphologies were examined



1 using a Nova NanoSEM 450 scanning electron microscope. Transmission electron
2 microscopy (TEM) was performed with a JEOL-2100 to investigate the internal
3 structure and layered morphology of the persimmon-derived sample.
4 Thermogravimetric analysis (TGA) for thermal stability, Raman spectra were obtained
5 using a Renishaw InVia Raman microscope equipped with a 514 nm laser to analyze
6 the defect structure in the synthesized PrGO. X-ray photoelectron spectroscopy (XPS)
7 was carried out using a K-Alpha spectrometer (Thermo Fisher Scientific, USA) to
8 analyze surface functional groups and elemental composition. As a surface-sensitive,
9 photoelectric effect-based technique, XPS provides quantitative information about the
10 elemental composition and chemical states present on the sample surface.

11

12 *3.2. Electrodes preparation and electrochemical analysis*

13 The material's electrochemical behavior was investigated in three (with 1M
14 H₂SO₄, 6M KOH, 2M KCl) and two-electrode configurations (with H₂SO₄) in the
15 Metrohm Auto lab electrochemical workstation. PrGO was used as working electrodes,
16 Pt wire as counter, and Ag/AgCl as reference electrode in a three-electrode setup. The
17 working electrode was made by coating a graphite sheet (1 × 1 cm²) with a combination
18 of 90% PrGO and 10% polyvinylidene fluoride (PVDF). For this PrGO was dissolved
19 in NMP solvent, and then using a mortar and pestle PVDF was gradually added to
20 generate this homogenous slurry. Next, this slurry of the produced material was applied
21 to 1 × 1 cm² graphite sheets and dried at 80 °C to create a working electrode. The mass
22 of the active substance in the electrode was around 1 mg. The symmetric supercapacitor
23 device with PrGO as an electrode material was subjected to electrochemical
24 experiments using a two-electrode setup. The symmetric supercapacitor device with
25 PrGO as an electrode material was built using two identical electrodes that had the same
26 mass (1 mg) of PrGO. Between the electrodes, Whatman filter paper, a porous separator
27 was used, to keep the circuit from shorting out while yet letting ions pass through. The
28 electrodes were configured in a sandwich arrangement with a 1M H₂SO₄ aqueous
29 electrolyte, ensuring adequate electrolyte volume to completely saturate both electrodes
30 and the separator. The device was then encased in a Swagelok-type arrangement to
31 maintain uniform pressure and avert electrolyte evaporation. This stringent assembly



1 methodology guarantees that the documented internal resistance and cycling stability
 2 accurately represent the practical performance of the PrGO material. View Article Online
DOI: 10.1039/D6TA01141A

3

4 CV analysis was performed to investigate the electrochemical properties of
 5 PrGO over an optimized voltage range. The following equation was used to compute
 6 the specific capacitance (C_s) from CV curves:

$$7 \quad C_s = \frac{A}{2mKV} \quad (1)$$

8

9 Additionally, GCD tests were carried out at varied current densities across fixed
 10 voltage ranges to assess the charging-discharging performance and the cyclic stability
 11 of the as-prepared materials and constructed supercapacitor cell. The C_s based on the
 12 GCD was calculated by Eq. 2:

$$13 \quad C_s = \frac{I\Delta t}{m\Delta V} \quad (2)$$

14

15 The two key factors that define the performance of the SCs are energy and power
 16 density. How much energy a gadget holds is referred to as energy density. The
 17 following formula was used to get the energy density:

$$18 \quad E = \frac{1}{2} \times C(\Delta V)^2/3.6 \quad (3)$$

19

20 How rapidly a device can discharge its energy is referred to as a SC's power density.
 21 The above formula was used to determine the power density (PD) of the constructed
 22 gadget.

$$23 \quad PD = \frac{E \times 3600}{\Delta t} \quad (4)$$

24 Device capacitance and cyclic stability are shown by the most likely rectangular CV
 25 curve. GCD measurements were taken at varied current densities in the potential
 26 window 0 to 1 V. Charging and discharging processes cause galvanostatic
 27 charge/discharge curves to rise and then fall. Device impedance was measured using
 28 EIS data.

29 In the above equations C_s , A , m , k , V , Δt , ΔV , C , and E represent the specific
 30 capacitance, absolute surface area covered by the CV curve, mass of coated electrode
 31 material (in mg), scan rate (in mV/s), the voltage difference between the CV curves (V_2



1 - V_1), discharging period in seconds, potential window, specific capacitance at a certain
2 current density and energy density of the device at a particular current density,
3 respectively.

4. Results and discussion

4.1. Optimization of carbonization temperature and heating rate

7 The carbonization temperature and heating rate are critical parameters governing the
8 yield, structural evolution, and graphitic ordering of biomass-derived carbon materials.
9 Therefore, a systematic optimization was carried out to identify conditions that balance
10 material yield with desirable structural characteristics for electrochemical applications.

11 TGA was first employed to examine the thermal decomposition behavior and carbon
12 yield of the persimmon-derived hydrogel as a function of carbonization temperature
13 (**Fig. 1(a)**). The results indicate a progressive decrease in the yield of the pyrolysis
14 product with increasing final temperature, declining from 41.4% at 600 °C to 21.7% at
15 1000 °C. This trend is attributed to enhanced devolatilization, cleavage of oxygen-
16 containing functional groups, and aromatization at elevated temperatures, which
17 collectively promote mass loss. While lower temperatures preserve higher yields,
18 insufficient carbonization limits structural ordering. Conversely, excessively high
19 temperatures lead to pronounced material loss without proportionate improvements in
20 graphitic structure. Based on this balance, 800 °C was identified as an optimal
21 carbonization temperature, providing an acceptable yield (34.67%) while ensuring
22 effective thermal reduction and carbon framework development.

23 The structural evolution of the carbon materials obtained at different temperatures was
24 further evaluated using Raman spectroscopy (**Fig. 1(b)**). All pyrolyzed samples
25 exhibited the characteristic D band ($\sim 1350\text{ cm}^{-1}$) and G band ($\sim 1592\text{ cm}^{-1}$),
26 corresponding to defect-induced disorder and in-plane stretching of sp^2 -hybridized
27 carbon, respectively. With increasing carbonization temperature, a gradual
28 enhancement in the intensity of the G band and improved definition of the Raman
29 features were observed, indicating progressive structural ordering. However, the
30 persistence of a prominent D band across all temperatures reflects the retention of
31 defects and edge sites, which are typical of reduced graphene oxide-like materials



1 derived from biomass precursors. Notably, the spectral evolution from 800 °C to higher
2 temperatures showed only marginal improvements, suggesting that further thermal
3 treatment does not significantly enhance graphitization.

4 Complementary insights into the long-range structural ordering were obtained from
5 XRD analysis (**Fig. 1(c)**). The XRD patterns display a broad diffraction peak centered
6 around $2\theta \approx 24^\circ$, characteristic of the (002) plane of turbostratic or disordered graphitic
7 carbon. Increasing the carbonization temperature resulted in a modest increase in peak
8 intensity and slight narrowing up to 800 °C, indicative of improved stacking and partial
9 graphitic ordering. Beyond this temperature, no substantial changes in the diffraction
10 profiles were observed, confirming that higher thermal treatment does not yield
11 significant structural benefits.

12 After establishing 800 °C as the optimal carbonization temperature, the influence of
13 heating rate on carbon yield was investigated by TGA at ramp rates of 5, 10, and 15 °C
14 min^{-1} (**Fig. 1(d)**). The lowest heating rate (5 °C min^{-1}) resulted in a substantially
15 reduced yield (18.2%), which can be attributed to prolonged exposure to intermediate
16 temperatures, leading to excessive decomposition and volatilization. In contrast, higher
17 heating rates of 10 and 15 °C min^{-1} significantly improved the yield to 34.39% and
18 36.82%, respectively. As the difference in yield between these two rates was minimal,
19 a heating rate of 10 °C min^{-1} was selected as an optimal condition, offering controlled
20 carbonization while minimizing unnecessary mass loss.

21 Based on the combined TGA, Raman, and XRD analyses, the optimized synthesis
22 conditions were established as carbonization at 800 °C with a heating rate of 10 °C
23 min^{-1} , followed by a dwell time of 60 min and controlled cooling of 2 °C/min. The
24 resulting material, denoted as PrGO, exhibits a reduced graphene oxide-like structure
25 with favorable defect density and partial graphitic ordering, making it well suited for
26 electrochemical energy storage applications. Although the carbonization temperature
27 was optimized based on structural evaluation and material yield, and the
28 electrochemical performance of the optimized sample was subsequently investigated in
29 acidic, neutral, and basic electrolytes, while a systematic comparison with other
30 temperatures will be explored in future work.

31



4.2. Structural and Chemical Characterization of Optimized PrGO

View Article Online
DOI: 10.1039/D6TA01141A

Following the optimization of the carbonization temperature and heating rate, the structural and chemical properties of the optimized PrGO, synthesized at 800 °C with a heating rate of 10 °C min⁻¹, were systematically investigated to elucidate its reduced graphene oxide-like nature and potassium incorporation.

Raman spectroscopy provided insights into the structural characteristics of graphene-based materials.^{33,34} The data showed the presence of two characteristic bands i.e. D & G band located at wavenumber of 1350 cm⁻¹ and 1592 cm⁻¹, respectively with the ID/IG ratio of 0.90 (**Fig. 1(e)**). The D band is associated with structural instability, while the G band is caused by the stretching of carbon sp² atoms.^{35,36} Two additional bands are observed around 2700 and 2900 cm⁻¹, corresponding to the 2D band and the (D + G) combination mode, respectively. These two supplementary bands originated from the imperfections found in the graphitic arrangement of the carbon substance.

Raman spectroscopy was further analyzed to explicitly examine the characteristics of the 2D band. The Raman spectrum of PrGO shows a discernible 2D band centered at ~2708 cm⁻¹. Peak deconvolution (Gaussian fitting) reveals that the 2D band exhibits a large full width at half maximum (FWHM) of ~317 cm⁻¹, indicating significant structural disorder. The 2D band is broad and of low intensity relative to the G band, suggesting that the material does not consist of single-layer graphene. Instead, the pronounced broadening and reduced intensity of the 2D peak indicate the presence of few-layer graphene with turbostratic stacking and limited long-range order, which is characteristic of reduced graphene oxide-like (rGO-like) carbon materials.

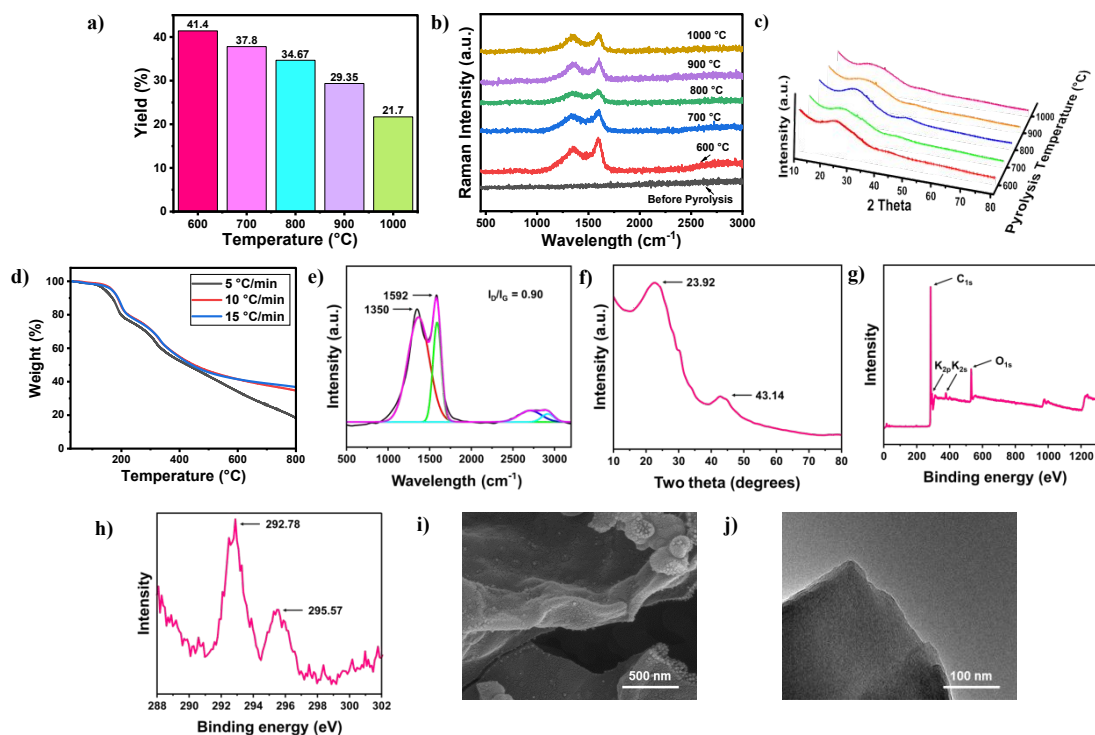
Furthermore, the ID/IG ratio of 0.90 supports the presence of defect-rich graphene-like domains. This value falls within the optimal range (0.8–1.0) reported for biomass-derived graphene-like materials used in supercapacitor applications, where a balanced degree of disorder enhances electrochemical performance.³⁷

This structural disorder can be attributed to the partial retention of oxygen-containing functional groups and defect formation during the pyrolysis of the persimmon-derived hydrogel. Such functional groups disrupt the continuity of the sp² carbon network by introducing vacancies, edge defects, and local lattice distortions,



1 thereby enhancing the D-band intensity. Consequently, the Raman results indicate that
 2 the disordered structure of PrGO originates from defect sites associated with residual
 3 functional groups and imperfect graphitic domains formed during thermal conversion.

4



5

6 **Fig. 1.** (a) Residual yield as a function of pyrolysis temperature; (b) Raman spectra and
 7 (c) XRD patterns of samples pyrolysis at different temperatures (600–1000 °C); (d)
 8 TGA curves at different heating rates (5–15 °C min⁻¹). Data for PrGO synthesized
 9 under optimized conditions (800 °C and 10 °C min⁻¹): (e) Raman spectrum, (f) XRD
 10 pattern, (g) XPS survey spectrum, (h) high-resolution K 2p XPS spectrum, (i) SEM
 11 image (500 nm), and (j) HR-TEM image (100 nm).

12

13

14

15

16

17

18

19

20

The XRD was used to analyze the crystallinity or amorphous nature of the produced PrGO. After undergoing pyrolysis (thermal reduction), a broad peak becomes visible for PrGO at a 2θ value of 23.92° (**Fig. 1(f)**). This suggests that the pi-conjugated structure of graphene has been significantly restored in PrGO and the broad peak (002) reflects a random crystal phase.^{6,9} The material's random arrangement during the formation of a few layers of PrGO via pyrolysis, specifically a broad peak at $2\theta = 23.92^\circ$ in XRD, strongly correlated with the D band observed in the Raman data. This correlation can be attributed to the disorderness of the PrGO.³⁸



1 To determine the sample thickness and number of layers it contains, Scherrer's
2 and Bragg's equations were used, as detailed in prior studies.³⁹⁻⁴¹ To determine the
3 number of layers, divide the crystal size (C) by the layer interlayer distance (d) and then
4 add one.³⁹⁻⁴² The crystal size (C) of the material has been calculated as 2.32 nm using
5 the diffraction peak at $2\theta = 23.92^\circ$. The interlayer spacing (d) of the PrGO material,
6 determined from this peak, is 0.67 nm. This value is significantly larger than the typical
7 interlayer distance of reduced graphene oxide (rGO), which generally ranges from
8 ~ 0.34 to 0.39 nm. The increased interlayer distance in PrGO can be attributed to the
9 swelling nature of the biomass precursor. During the initial hydrothermal treatment
10 followed by freeze-drying, the precursor structure is plausible retained, and subsequent
11 thermal exfoliation in the second heating step (800 °C) further increases the spacing
12 between graphene-like layers. The XRD results indicate the presence of a few layers—
13 about 3–4 layers of graphene in PrGO. It was also discovered that the thin rGO
14 nanosheets were stacked together, forming a thick, layered structure due to significant
15 Van der Waals interactions between layers.⁴³ Another less intense peak at $2\theta = 43.14^\circ$
16 with (001) orientation was associated with the turbostratic band of disorganised carbon
17 materials.³⁸

18 The BET results of the samples before and after pyrolysis at 800 °C reveal a
19 69.8% increase in specific surface area, rising from 37.1 m²/g to 63.0 m²/g after
20 pyrolysis (**ESI†, Fig. S2**). This indicating the development of a more accessible surface
21 upon thermal treatment and additional porosity within the carbon framework.

22 Although the obtained surface area is moderate, this can be attributed to the restacking
23 of graphene layers; however, it remains consistent with biomass-derived rGO
24 materials.^{44,45} For instance, oil palm waste-derived rGO has been reported to exhibit
25 relatively low surface areas (as low as 8–15 m²/g) due to restacking and blocked pores,
26 despite successful graphitization.⁴⁴ Similarly, basil seed (*Ocimum basilicum* L.) derived α -
27 Fe₂O₃/ZnO, rGO-like carbon shows moderate surface area of 24.569 m²·g⁻¹.⁴⁵

28 In addition, the total pore volume increases from 0.14 to 0.17 cm³/g, further confirming
29 the formation of an expanded pore network. The average pore diameter decreases from
30 15.53 nm to 10.77 nm, indicating the development of a more refined mesoporous
31 structure (**ESI†, Fig. S2**). A mesoporous architecture of PrGO is beneficial for
32 supercapacitor applications, as it facilitates efficient ion diffusion and minimizes

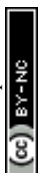


1 transport resistance. The increased surface area provides more active sites for charge
2 accumulation, while the interconnected mesopores enhance electrolyte accessibility
3 and ion mobility.

4 The full scan XPS measurements of PrGO indicate the presence of carbon,
5 oxygen, and potassium with atomic percents of 88.41, 9.05, and 2.15, respectively. **Fig.**
6 **1(g)** displays the XPS full-scan, with C1s, O1s, K₂p_{3/2}, K₂p_{1/2}, and K2s peaks located
7 at 284.50 eV, 531.78 eV, 292.08 eV, 295.57 eV and 378.9 eV.²¹ **Fig. 1(h)** shows two
8 different peak satellites corresponding to K₂P_{3/2} and K₂P_{1/2} at 292.93 eV and 295.70 eV,
9 respectively.⁴⁶ Four peaks from the deconvolution of C1s spectra have been positioned
10 at 284.50 eV, 286.10 eV, 292.71 eV, and 295.74 eV. The strength of the peaks at 284.50
11 eV is higher, indicating that PrGO is mostly associated with sp² hybridization (C=C)
12 and confirming the presence of a pi network in the synthesised PrGO. The peak at
13 286.10 eV is attributed to C–O functional groups, while the higher binding energy
14 features at 292.71 and 295.74 eV are assigned to π–π* shake-up satellite transitions
15 associated with aromatic sp² carbon domains (**ESI†, Fig. S3**). The binding energy
16 values for O1s revealed that oxygen exists in two distinct chemical environments, with
17 C=O at 530.86 eV and C–O at 532.30 eV (**ESI†, Fig. S4**).

18
19 The FTIR spectrum of PrGO exhibits key vibrational features indicative of potassium-
20 coordinated oxygen functionalities. A broad band centred at 1566 cm⁻¹ corresponds to
21 the asymmetric stretching vibration of the carboxylate group, while a weaker band at
22 1378 cm⁻¹ is assigned to the symmetric COO⁻ stretching. A very small and broad peak
23 in the 1700–1730 cm⁻¹ region suggests that most carboxylic acid groups have been
24 deprotonated, confirming the formation of potassium carboxylate (COO⁻K⁺) species.
25 Additionally, a broad and intense peak around 1200 cm⁻¹ is attributed to overlapping
26 contributions from C–O–C asymmetric stretching and C–O vibrations of residual
27 oxygen-containing groups, potentially stabilized by potassium coordination (**ESI†, Fig.**
28 **S5**). TGA analysis was performed to study the thermal stability of the material. TGA
29 data shows two stage thermal decomposition. In first stage (up to 380 °C) the less
30 weight loss was observed due to the removal of absorbed water molecules or physically
31 attached functional groups while the second stage weight loss (temperature higher than
32 380 °C) was due to decomposition the material (**ESI†, Fig. S6**)

33



1 4.3. Surface properties

View Article Online
DOI: 10.1039/D6TA01141A

2 SEM analysis was performed to examine the surface morphology of the PrGO. As
3 shown in **Fig. 1(i)**, at a magnification of 500 nm, the material exhibits a distinct sheet-
4 like structure. To further analyze the surface features, a 3D surface plot and roughness
5 measurements were generated using ImageJ software ((ESI†, **Fig. S7(a–d)**). **Fig. S7(a)**
6 was used to generate a hill stack view of the surface, shown in **Fig. S6(b)**, which
7 displays the uneven arrangement of graphene sheets with varying sheet areas, curling
8 edges, and sharp spikes. The presence of these morphological defects results in a higher
9 defect concentration, enhancing the metallic properties of the nanosheets and
10 contributing to their excellent conductivity.

11 The 3D surface plot of the selected area of **Fig. S7(c)**, shown in **Fig. S7(d)**, further
12 highlights the corrugated edges and the interconnected stacking of graphene sheets,
13 held together by Van der Waals forces. Such surface roughness and structural
14 irregularities are expected to increase ion accessibility and thus significantly enhance
15 the material's capacitive performance. The SEM observations are consistent with the
16 FT-IR, Raman, and XRD results, all of which confirm the formation of few-layered
17 PrGO sheets. Finally, a supercapacitor was fabricated using PrGO as the electrode
18 material to validate its promising capacitive behaviour.

19 The internal morphology of the PrGO was obtained by HR-TEM analysis. High
20 resolution TEM images shows the sheet like structure of the PrGO **Fig. 1(j)**. **Fig. S8(a-
21 c)** revealed the presence of 3–4 layers in PrGO, which also resembled the XRD findings.
22 The hill stack plot diagram in HR-TEM at 50 nm magnification (**Fig. S7(d)**) reveals the
23 rough surface of the nanosheets, which have ridged edges that make them well-suited
24 for supercapacitor applications. The data on surface roughness aligns well with the
25 SEM results. In addition, **Fig. S8(e)** presents a 3D surface plot of the highlighted region
26 of the HR-TEM image, generated using the Fire LUT in ImageJ. In this plot, darker
27 blue regions correspond to lower height values, typically only a few nanometers, while
28 lighter regions represent higher surface features. A colour scale bar has also been added
29 to provide a quantitative reference for these height variations, further highlighting the
30 grain boundaries and layered structure within the sample.

31 32 5. Electrochemical performance of the PrGO



5.1. Cyclic voltammetry (CV)

The electrochemical study of PrGO was initially evaluated using a 3-electrode system with 1 M H₂SO₄ as the electrolyte. The CV curves with the potential range of -0.1 to 1.1 V are displayed in **Fig. 2(a)**. A different scan rates 2, 5, 10, 20, 50, 100, and 200 mV/s were used to determine the Cs of PrGO. The results of these measurements were about 302, 284, 260, 209, 146, 109, and 60 F/g, respectively (**Table-1**).

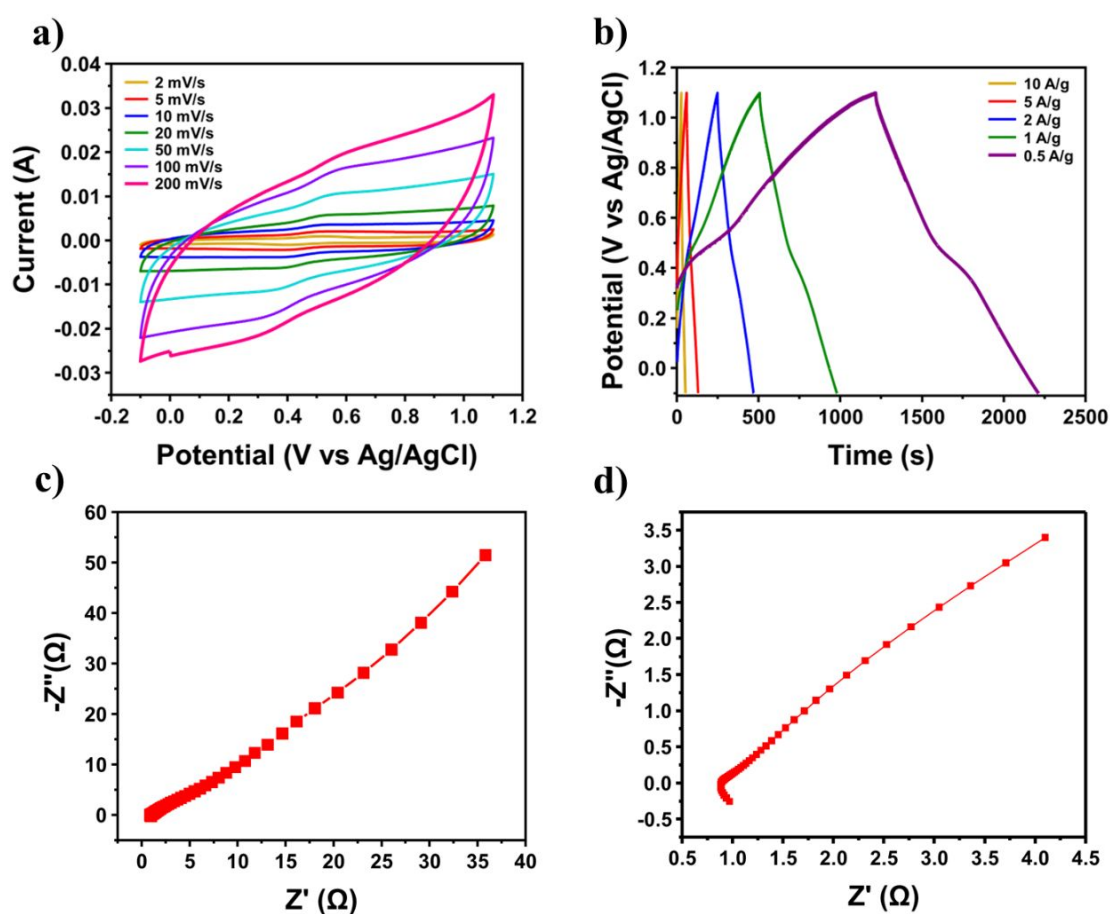


Fig. 2. (a) CV plots at numerous scan rates, (b) GCD at different current densities, (c) Nyquist plot, and (d) Magnified view of the Nyquist plot.

It was noticed that the CV curves retained a quasi-rectangular shape over the entire range of scan rates, indicating dominant electric double-layer capacitance (EDLC) behavior. Although the specific capacitance decreased with increasing scan rate due to diffusion limitations of electrolyte ions at higher rates, the overall shape preservation confirms good rate capability and efficient charge-storage kinetics.



1 **Table 1.** The specific capacitance of PrGO at different scan rates.View Article Online
DOI: 10.1039/D6TA01141A

Scan Rate (mV/s)	2	5	10	20	50	100	200	
Specific Capacitance (F/g)	1M H ₂ SO ₄	302.08	284.16	260.10	209.58	146.54	109.29	60.79
	2M KCl	293.12	223.14	178.32	135.61	80.05	54.10	36.45
	6M KOH	152.55	100.23	69.12	51.15	35.35	26.42	19.42

2

3 *5.2. Galvanostatic charge/discharge (GCD)*

4 The supercapacitive behaviour of the produced electrode was extensively
5 investigated through GCD tests. These tests were conducted at current densities,
6 ranging from 0.5 to 10 A/g, within a potential window of -0.1 to 1.1 V. **Fig. 2(b)**
7 displayed GCD profiles for PrGO at different current densities, while keeping the
8 potential constant at 1.2 V. The material exhibited a higher Cs of 412 F/g at a current
9 density of 0.5 A/g. Although the current density was raised, the Cs experienced a slight
10 decrease to 215 F/g at 10 A/g (**Table-2**). The material demonstrated excellent
11 capacitance and impressive rate capacity in terms of its GCD behavior. The low
12 resistance of ion transport and the short diffusion distance during the charging-
13 discharging process contribute to this phenomenon.

14 **Table 2.** The specific capacitance of PrGO at different current densities.

Current density (A/g)	0.5	1	2	5	10	
Specific Capacitance (F/g)	1M H ₂ SO ₄	412.70	396.33	369.70	298.00	215.00
	2M KCl	192.42	143.12	94.22	67.31	-
	6M KOH	46.12	34.02	22.54	15.33	-

15

16 *5.3. Electrochemical impedance spectroscopy (EIS)*

17 The EIS analysis was performed to assess the internal resistance/impedance of
18 the material, as well as to examine the diffusion kinetics and transportation behavior of



1 electrolyte ions. This analysis utilized a 1M H₂SO₄ electrolyte and covered a frequency
2 range of 10 mHz to 10⁶ Hz. The Nyquist plot, shown in **Fig. 2(c)**, depicts the
3 relationship between the real impedance (Z') and the imaginary impedance (Z'') of
4 various devices. It is worth noting that the plot exhibits a rising trend in the low-
5 frequency range, which suggests the capacitive characteristics of the synthesized
6 material. In general, the Nyquist plot consists of a semicircle along with a straight line
7 at a 90-degree angle. This semicircle symbolizes the charge-transfer-resistance (R_{ct})
8 that exists between the electrode and electrolyte. The **Fig. 2(d)** clearly illustrates a small
9 semi-circular region in the plot, which suggests that there may be low faradaic
10 resistances in the electrolyte. The intersection point of the X-axis in the EIS plot, known
11 as the Nyquist plot, is referred to as the equivalent series resistance (ESR). The ESR
12 encompasses several factors, including the resistance of materials, the resistance of
13 electrolytic ions, and the resistance at the contact point between the current collector
14 and the electrode material. The material exhibited a significantly low internal resistance
15 of $R_{eq} = 0.96 \Omega$ in the higher frequency range, indicating its great conductivity and
16 superior electrochemical performance.

17 To further understand the influence of electrolyte environment, the
18 electrochemical performance of PrGO was additionally investigated in neutral (2 M
19 KCl) and alkaline (6 M KOH) electrolytes. The corresponding CV, GCD, and EIS
20 profiles are provided in **ESI†**, **Fig. S9** and **Fig. S10**, while the calculated specific
21 capacitance values are summarized in Table 1 and Table-2. Compared to the acidic
22 medium, a gradual decrease in capacitance is observed in neutral and alkaline
23 electrolytes, which can be attributed to the lower ionic conductivity, larger hydrated
24 ionic radius, and slower diffusion kinetics of K⁺ ions. These results confirm the strong
25 dependence of electrochemical performance on electrolyte properties.

26 5.4. Electrochemical performance of the device

27 Additionally, in order to assess its feasibility in real-time supercapacitors, we
28 have constructed a symmetric SC device using an aqueous 1 M H₂SO₄ electrolyte and
29 study its performance using CV, GCD, and EIS techniques. **Fig. 3 (a)** displays the CV
30 curves obtained from the fabricated device using the synthesized material. The
31 measurements were conducted at various scan rates ranging from 2 to 200 mV/s within
32 a potential range of 0 to 0.9 V. All of the CV curves displayed a leaf-like shape that

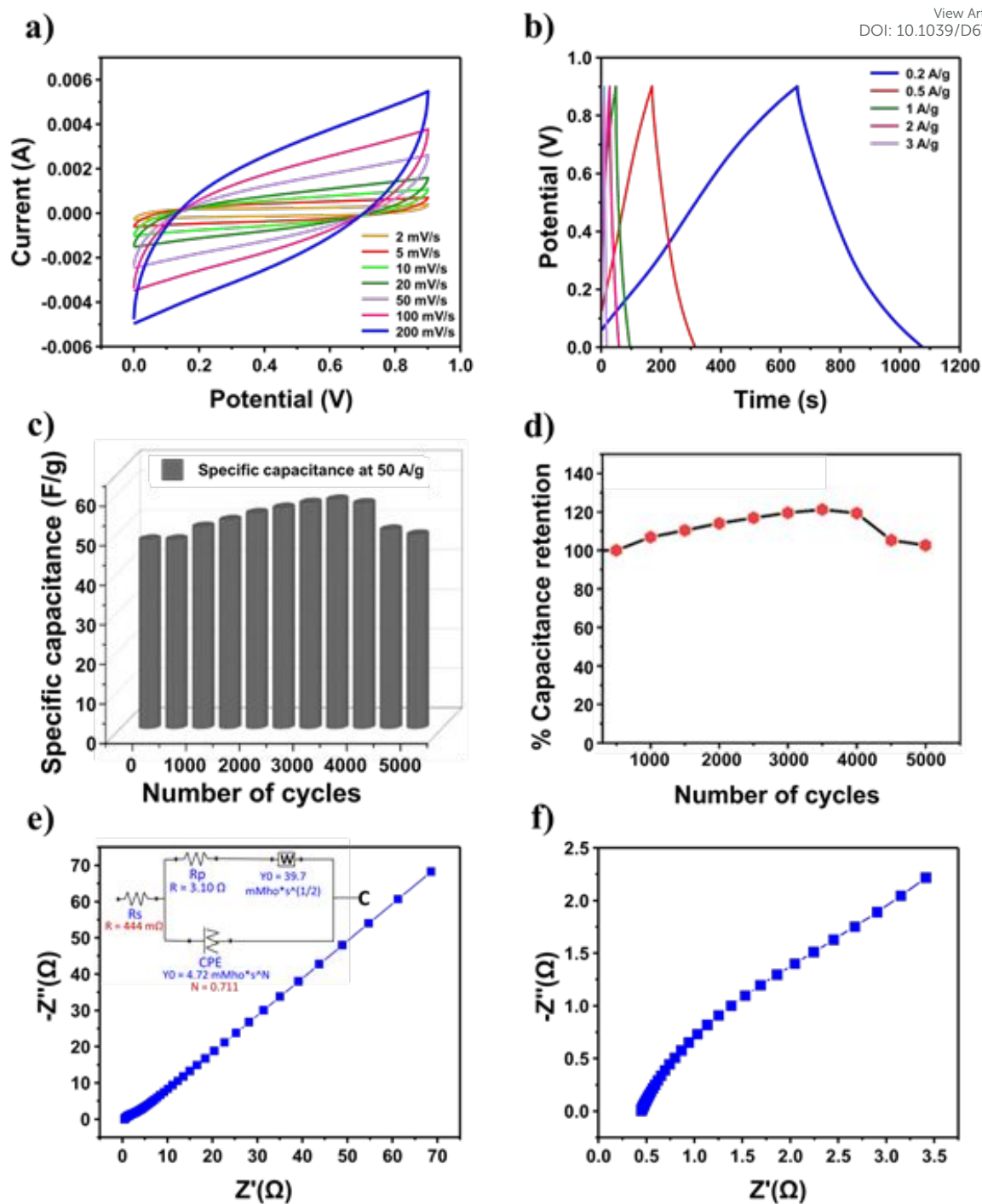


1 was similar. The Cs of the fabricated device was calculated at different scan rates of 2
2 to 200 mV/s and obtained values of Cs are listed in **Table-3**. Furthermore, the device
3 underwent GCD experiments, where current densities ranged from 0.2 A/g to 3 A/g.
4 **Fig. 3(b)** displays the device-specific capacitances at different current densities. The
5 calculated capacitance for different current densities is given in **Table-4**.

6 One notable advantage of supercapacitor is their long-term cyclic stability. In
7 order to ensure the stability of a SC device over a large number of cycles, it is essential
8 to conduct a cyclic stability test. **Fig. 3(c)** illustrates the cyclic stability of the device in
9 terms of Cs and percentage capacitance retention. The device was tested within a
10 potential window of 0 to 0.9 V at a high current density of 50 A/g for 5000 cycles in a
11 1 M H₂SO₄ solution. Based on the information provided in **Fig. 3(d)**, it is evident that
12 the device exhibits a capacitance retention of 78% after undergoing 5000 cycles.
13 Although traditional EDLCs generally demonstrate over 90% capacitance retention, the
14 approximately 78% retention reported in our K-doped rGO-like material can be
15 ascribed to several causes. The first is the substantial contribution to pseudocapacitance
16 brought about by potassium doping and residual oxygen functional groups.
17 Nevertheless, compared to pure electrostatic charge storage, these faradaic processes
18 are intrinsically less stable, and capacitance fading occurs as a result of the irreversible
19 redox consumption of surface functional groups during cycling.⁴⁷ The second point is
20 that with an acidic electrolyte (H₂SO₄), the active K-sites and large surface area can
21 cause the electrolyte to decompose locally at the electrode interface or even evolve into
22 gas (H₂/O₂ evolution). This would lead to micropore blockage and an increase in
23 internal resistance during prolonged cycling.⁴⁸ Thirdly, the effective accessible surface
24 area decreases over continuous cycling due to partial pore blockage or ion entrapment,
25 especially within micropores, in the hierarchical porous structure.⁴⁹ The apparent trade-
26 off between high capacitance and moderate cycling stability is accounted for by these
27 combined effects.

28





1
 2 **Fig. 3.** (a) CV plots at numerous scan rates, (b) GCD plot at numerous current densities,
 3 (c) Cyclic stability, (d) % Capacitance retention of fabricated SC device, (e) Nyquist
 4 plot of PrGO derived SC device (inset: equivalent circuit model used for fitting), and
 5 (f) Magnified view of the Nyquist plot.

6
 7 **Table 3.** The specific capacitance of PrGO at different scan rates.

Scan Rate (mV/s)	2	5	10	20	50	100	200
---------------------	---	---	----	----	----	-----	-----



Specific Capacitance (F/g)	161.02	130.42	93.10	64.22	40.34	28.76	21.00
----------------------------	--------	--------	-------	-------	-------	-------	-------

View Article Online
DOI: 10.1039/D6TA01141A**Table 4.** The specific capacitance of PrGO at different current densities.

Current density(A/g)	0.2	0.5	1	2	3
Specific Capacitance (F/g)	98.00	82.20	72.00	59.05	43.20

The study utilized EIS to identify the equivalent sheet resistance (ESR) or cell internal resistance. The frequency range used for the study was 10 mHz to 10⁶ Hz. Based on the data from the **Fig. 3(e & f)**, we observed that the fabricated device exhibited a lower ESR value, approximately 0.65 ohms. The low equivalent series resistance (ESR) can be attributed to potassium-induced electronic modulation, where K acts as an n-type dopant, enhancing the electrical conductivity of the rGO framework. In addition, the expanded interlayer spacing and defect-rich structure improve electrolyte wettability and ion transport, thereby facilitating charge transfer kinetics and decrease resistance at the electrode/electrolyte contact.^{50,51} The synthesized material exhibits excellent supercapacitive performance as an electrode material for supercapacitors, as evidenced by its low ESR value. Furthermore, the device exhibits an energy density of approximately 11.0 Wh/kg, accompanied by a power density of 89.8 W/kg, when operating at a low current density of 0.2 A/g. The comparison of capacitance, power density (ES), and ESR values of PrGO with other graphene-based materials is given in the ESI† (Tables S2 and S3).

6. Computational analysis of PrGO

Density functional theory (DFT) based computational investigations have been performed to understand the structural, electronic and capacitive aspects of the PrGO. The computational PrGO material has been designed using the XPS data to closely mimic its experimental counterpart as shown in **Table-5**. Initially, the theory has been evaluated for the pristine graphene, thereafter utilized for the PrGO. The density functional simulations utilize Generalized Gradient Approximation (GGA) with Perdew-Burke-Ernzerhof (PBE) parameterization, along with Grimme-D2 Van der Waals correction.⁵² The high symmetry points of the Brillouin zone in the reciprocal space have been sampled with *k*-points of 30*30*1 and 7*7*1 for primitive cell of



1 pristine graphene having 2 atoms and supercell of PrGO having 54 atoms, respectively
 2 A sufficiently large k -points of $27 \times 27 \times 1$ have been utilized to accurately extract the
 3 density of states (DOS). The structural relaxations are performed using the limited
 4 memory Broyden–Fletcher–Goldfarb–Shanno (L-BFGS) algorithm to achieve the
 5 defined force and stress tolerances of 0.05 eV/\AA and 0.1 GPa , respectively.

6

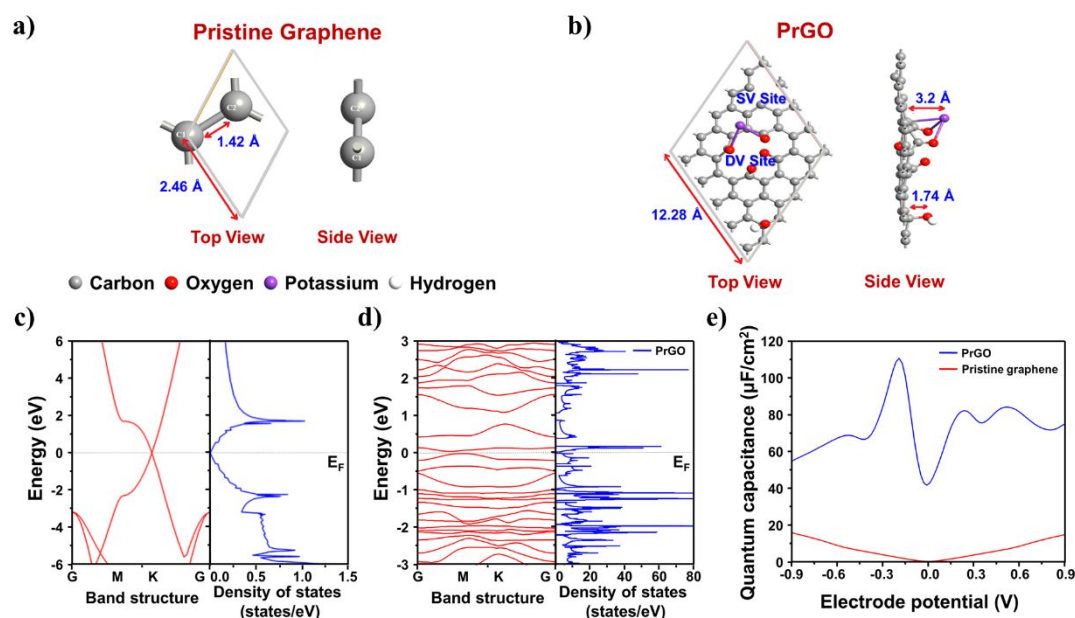
7 **Table 5.** The atomic composition of the PrGO.

Element	XPS Data	Computational Design
Carbon	88.41	87.03
Oxygen	9.05	9.25
Potassium	2.15	1.85
Miscellaneous	0.39 (Unknown)	1.85 (Hydrogen)

8

9 The relaxed atomic structures of simulated pristine graphene and PrGO are shown in
 10 **Fig.4.** Computationally, all the properties of pristine graphene can be extracted by
 11 simulating its primitive cell consisting of 2 atoms. The lattice constant and carbon-
 12 carbon bond length of pristine graphene are noted as 2.465 \AA and 1.42 \AA , respectively.

13



14

15 **Fig. 4.** The relaxed atomic structures of simulated (a)pristine graphene, (b) PrGO, The
 16 electronic band structure and density of states (DOS) profiles of (c) pristine graphene,



1 (d) PrGO (Here, the Fermi level is shifted to energy zero), and (e) Quantum capacitance
2 offered by pristine graphene and PrGO.

3
4 The computed electronic band structure and DOS profiles (**Fig.4(b)**) of pristine
5 graphene show a perfect Dirac cone shape (at the K-point of the Brillouin zone in band
6 structure). The investigation of partial DOS reveals that the states near to Fermi level
7 arise only from the p -states of carbon, which can be attributed to the aromaticity or
8 delocalization of π -cloud from the p_z -orbitals. While designing the PrGO nanosheet
9 (**Fig.4(c)**), a double vacancy (DV) defect has been created in the 5*5 supercell of
10 graphene to position four carbonyl (R=O) groups. A hydroxyl (R-OH) group is also
11 inserted into the supercell to achieve the targeted oxygen concentration. It has been
12 noted that all the carbon atoms associated with the carbonyl and hydroxyl groups have
13 slightly shifted out of plane indicating their hybridization transformation from sp^2 to
14 sp^3 . Our previous study indicated that substitutional doping of Potassium is more
15 favorable in the graphene,⁵³ thus the potassium is originally inserted at a single vacancy
16 (SV) site through substitutional doping prior to the structural relaxation. However, post
17 structural relaxation, the potassium atom is observed to vacate its most favorable SV
18 site in graphene and bond with the oxygen atoms of rGO. This can be attributed to the
19 very high electronegativity of oxygen (3.44 by Pauling scale) in comparison to
20 potassium (0.82 by Pauling scale). Thus, the potassium is most likely bonded with the
21 oxygens in the synthesized PrGO. The electronic band structure and DOS profile of
22 PrGO are shown in **Fig.4 (d)**, where large number of states are observed near to the
23 Fermi level in contrast to pristine graphene, which can be attributed to the presence of
24 defects and non-carbon elements. These large number of states have significant
25 influence on the quantum capacitance offered by the PrGO.

26
27 The quantum capacitance offered by pristine graphene and PrGO have been extracted
28 to understand their behavior as supercapacitor electrodes. Quantum capacitance is
29 inherent to the nano-materials due to the electronic compressibility and the low DOS.
30 The DOS ($D(E)$) dependent quantum capacitance (C_Q) is extracted using the MATLAB
31 programing⁵⁴ of the following expressions,^{55, 56}

32
33
$$C_Q = \frac{1}{V_e} \int_0^V C_Q^{diff}(V) dV \quad (5)$$



$$\text{Where, } C_Q^{diff} = \frac{e^2}{4KT} \int_{-\infty}^{\infty} D(E) \operatorname{sech}^2\left(\frac{E+V}{2KT}\right) dE$$

Here, V is the applied electrode voltage, e is elementary charge, E is energy, K is Boltzmann's constant, and T is temperature.

The computational quantum capacitance extracted for pristine graphene and PrGO as supercapacitor electrodes is depicted in **Fig. 4(e)**, where the values for pristine graphene are in good agreement with the experimental report by *Ponomarenko et al.*⁵⁷ The pristine graphene offers negligible quantum capacitance at zero potential, which increases gradually as the potential is varied, owing to its Dirac cone structure of DOS near the Fermi level. The maximum quantum capacitance offered by the pristine graphene within the considered electrochemical range is noted as 16.52 $\mu\text{F}/\text{cm}^2$ at -0.9 V. On the other hand, the PrGO offers substantially higher quantum capacitance than the pristine graphene portraying its suitability as supercapacitor electrode. The peak quantum capacitance offered by PrGO is noted as 110.75 $\mu\text{F}/\text{cm}^2$ at -0.19 V, which is about 6.7 times higher than pristine graphene. Moreover, the PrGO offers significant quantum capacitance on both the positive and negative sides of the electrochemical window predicting its suitability for symmetric supercapacitors.

7. Conclusion

In this study, few-layer reduced graphene oxide (rGO) was successfully synthesized from persimmon fruit using a clean, two-step thermal method. A systematic optimization of carbonization temperature and heating rate enabled the identification of suitable conditions for obtaining a conductive, graphene-like structure. The formation and quality of the rGO-like material (PrGO) were confirmed through comprehensive characterization techniques including Raman spectroscopy, XRD, FTIR, XPS, SEM, HR-TEM, and TGA. XPS analysis revealed a natural potassium doping level of 2.15 atomic percent, contributing to the material's enhanced electrochemical properties. The electrochemical performance of the synthesized material, i.e., PrGO, was investigated in three different electrolytes i.e. 1M H_2SO_4 (acidic), 2 M KCl (neutral) and 6 M KOH (alkaline) using a three-electrode setup. The maximum C_s achieved was 302 F/g at a



1 scan rate of 2 mV/s in acidic electrolyte. Additionally, a symmetric supercapacitor (SC)
2 device fabricated using PrGO achieved a high specific capacitance of 98 F/g, an energy
3 density of 11 Wh/kg, and a power density of 89.8 W/kg at a current density of 0.2 A/g.
4 The device also demonstrated excellent cycling stability, retaining 78% of its initial
5 capacitance after 5000 charge–discharge cycles. DFT-calculations were performed to
6 support the experimental results and assess the quantum capacitance behavior of PrGO.
7 While pristine graphene showed low quantum capacitance near zero potential, PrGO
8 exhibited a significantly higher value of 110.75 $\mu\text{F}/\text{cm}^2$ at -0.19 V—approximately 6.7
9 times greater than that of pristine graphene. Moreover, PrGO maintained appreciable
10 quantum capacitance across both positive and negative potentials, highlighting its
11 promise for symmetric supercapacitor configurations. Overall, this work demonstrates
12 the feasibility of producing potassium-doped, few-layer rGO from persimmon fruit as
13 a low-cost electrode material. The combined experimental and computational insights
14 underline its strong potential for high-performance supercapacitors and future
15 applications in energy storage technologies.

16
17

18 **Credit authorship contribution statement**

19 **Chetna Tewari**- conceptualization, methodology, experimentation, investigation, and
20 drafting the original manuscript, **Kundan Singh Rawat**- writing and reviewing the
21 manuscript, **Diksha Bhatt**- electrochemical analysis and contributed to the writing,
22 **Boddepalli SanthiBhushan and Anurag Srivastava**- computational analysis and
23 writing, **Young Nam Kim and Somi Yoon**- characterization. **Nanda Gopal Sahoo**-
24 electrochemical analysis and, review and editing of the manuscript, **Jun-Wei Zha**-
25 investigation, **Yong Chae Jung**- conceptual guidance, supervision, review and editing.

26

27 **Declaration of competing interest**

28 The authors declare that they have no known competing financial interests or personal
29 relationships that could have appeared to influence the work reported in this paper.

30

31 **Data availability**

32 Data will be made available on request.

33

34 **Acknowledgment**



1 The authors acknowledge National Research Council of Science and Technology (NSTC) New Article Online
DOI: 10.1039/D6TA01141A
2 grant from the governments of Korea (MSIT) (CRC23013-000), and KIST Institutional
3 Program for provided funding for this work.

5 References

- 6 1. Y. Shang, Y. Huang, L. Li, F. Wu, and R. Chen, *Chem. Rev.*, 2025, **125**, 5674–
7 5744. <https://doi.org/10.1021/acs.chemrev.4c00863>.
- 8 2. K.S. Rawat, C. Tewari, T. Arya, Y.N. Kim, P. Pant, S. Sati, S. Dhali, P.B. Negi,
9 Y.C. Jung, N.G. Sahoo, *Next Energy*, 2025, **6**, 100209.
10 <https://doi.org/10.1016/j.nxener.2024.100209>.
- 11 3. N. Choudhary, A. Tomar, S. Bhardwaj, J. Ćwiertnia, D. Just, D. Janas, R. Chandra,
12 P.K. Maji, *J. Mater. Chem. A*, 2025, **13**, 4012-4042.
13 <https://doi.org/10.1016/j.rser.2025.116624>
- 14 4. M. Murugan, G. Dineshkumar, K.C. Kumar, C. Tewari, M. Ganesan, N.G., Sahoo,
15 M. Sivanantham, *J. Electrochem. Soc.*, 2023, **170**, 040518. 10.1149/1945-
16 7111/acbf7b.
- 17 5. C. Tewari, Y.N. Kim, H. Muramatsu, M. Endo, Y.A. Kim, Y.C. Jung, *Langmuir*,
18 2023, **39**, 6698-6704. <https://doi.org/10.1021/acs.langmuir.3c00092>.
- 19 6. K.S. Rawat, C. Tewari, T. Arya, P. Pant, Y.N. Kim, R. Kumar, Y.C. Jung, and
20 N.G. Sahoo, *J. Power Sour.*, 2026, **661**, 238601.
21 <https://doi.org/10.1016/j.jpowsour.2025.238601>
- 22 7. P. Ponmani, J. Bahadur, C. Tewari, D.K. Gupta, U. Kalita, P. Jegadeesan, T.R.
23 Ravindran, A. Alex, A. Das, N.G. Sahoo, M. Sivanantham, *J. Polym. Sci.*, 2023,
24 **61**, 2149-2162. <https://doi.org/10.1002/pol.20220709>.
- 25 8. C. Tewari, K.S. Rawat, Y.N. Kim, T. Arya, S. Dhali, S. Rana, D.V. Andreeva, B.
26 Özyilmaz, R. Mahfouz, N. Qari, Y.C. Jung, N.G. Sahoo and K.S.
27 Novoselov, *Renew. Sustain. Energy Rev.*, 2026, **226**, 116443.
28 <https://doi.org/10.1016/j.rser.2025.116443>
- 29 9. J. Masa, and W. Schuhmann, *Chem. Cat. Chem.*, 2019, **11**, 5842-5854.
30 <https://doi.org/10.1002/cctc.201901151>
- 31 10. A. Morengi, S. Scaravonati, G. Magnani, M. Sidoli, L. Aversa, R. Verucchi, G.
32 Bertoni, M. Riccò, D. Pontiroli, *Electrochimica Acta*, 2022, **424**, 140626.
33 <https://doi.org/10.1016/j.electacta.2022.140626>.



- 1 11. T. Khandaker, T. Islam, A. Nandi, M.A.A.M. Anik, M.S. Hossain, M.K. Hasan, M.S. Hossain, *Sustain. Energy Fuels*, 2025, **9**, 693-723. <https://doi.org/10.1039/D4SE01393J>. View Article Online
DOI: 10.1039/D6TA01141A
- 2
- 3
- 4 12. K. Radhakrishnan, and A. Kumar, *Renew. Sustain. Energy Rev.*, 2026, **229**, 116624. <https://doi.org/10.1016/j.rser.2025.116624>
- 5
- 6 13. M. Cao, Y. Hu, W. Cheng, S. Huan, T. Bai, Z. Niu, Y. Zhao, G. Yue, Y. Zhao, G. Han, *Chem. Eng. J.*, 2022, **436**, 135233. <https://doi.org/10.1016/j.cej.2022.135233>.
- 7
- 8 14. D.C. Wang, H.Y. Yu, Z. Ouyang, D. Qi, Y. Zhou, A. Ju, Z. Li, Y. Cao, *Nanoscale*, 2022, **14**, 5163-5173 <https://doi.org/10.1039/D2NR00030J>
- 9
- 10 15. O. Akhavan, K. Bijanzad, A. Mirsepah, *RSC Adv.* 2014, **4**, 20441-20448. <https://doi.org/10.1039/C4RA01550A>.
- 11
- 12 16. G. Tatrari, C. Tewari, M. Pathak, M. Karakoti, B.S. Bohra, S. Pandey, B. SanthiBhushan, A. Srivastava, A. Rana, N.G. Sahoo, *J. Energy Storage*, 2022, **53**, 105098. <https://doi.org/10.1016/j.est.2022.105098>.
- 13
- 14
- 15 17. I. Berktaş, M. Hezarkhani, L. Haghighi Poudeh, B. Saner Okan, *Graphene Technol.*, 2020, **5**, 59-73. <https://doi.org/10.1007/s41127-020-00033-1>.
- 16
- 17 18. Y. Shen, *Renew. Sustain. Energy Rev.*, 2026, **225**, 116206. <https://doi.org/10.1016/j.rser.2025.116206>
- 18
- 19 19. S. Kumar, C. Tewari, N.G. Sahoo, L. Philip, *J. Hazard. Mater.* 2022, **435**, 128956. <https://doi.org/10.1016/j.jhazmat.2022.128956>.
- 20
- 21 20. L.E.Chaney, J. Hui, H. You, Y. Zhou, J.R. Downing, W.Y. Chen, E. Benson, J.B. Dunn, S.J. Rowan, and M.C. Hersam, *npj Advanced Manufacturing*, 2026, **3**, 3. <https://doi.org/10.1038/s44334-025-00063-8>
- 22
- 23
- 24 21. X. Su, L. Ge, S. Huang, X. Wang, H Xie, Y. Liu, L. Yi, L. Liu, J. Meng, and H. Meng, *Biomass and Bioenergy*, 2026, **208**, 108876. <https://doi.org/10.1039/D5NA00705D>
- 25
- 26
- 27 22. C. Tewari, Y. Kim, Y.N. Kim, S. Ryu, H.S. Jeong, Y.C. Jung, *J. Vinyl Addit. Technol.*, 2023, **30**, 102-113. <https://doi.org/10.1002/vnl.22032>.
- 28
- 29 23. H.R. Barai, N.S. Lopa, P. Barai, M.M. Rahman, A.K. Sarker, S.W. Joo, *J. Mater. Sci.: Mater. Electron.*, 2019, **30**, 21269-21277. [10.1007/s10854-019-02500-9](https://doi.org/10.1007/s10854-019-02500-9).
- 30
- 31 24. M. Liu, J. Niu, Z. Zhang, M. Dou, F. Wang, *Nano Energy*, 2018, **51**, 366-372. <https://doi.org/10.1016/j.nanoen.2018.06.037>.
- 32
- 33 25. Q. Li, X. Ye, Y. Jiang, E.H. Ang, W. Liu, Y. Feng, X. Rui, Y. Yu, *Mater. Chem. Front.*, 2021, **5**, 3132-3138. <https://doi.org/10.1039/D0QM00990C>.
- 34



- 1 26. F. Nathania, T. Nurkhoeriyati, 2025 Drying technologies utilized to preserve
2 persimmon fruits (*Diospyros kaki* L.): A review. In *IOP Conference Series: Earth
3 and Environmental Science* (Vol. 1445, No. 1, p. 012004). IOP Publishing.
- 4 27. A. Celik, S. Ercisli, *Int. J. Food Sci. Nutr.* 2008, **59**, 500-606.
5 <https://doi.org/10.1080/09637480701538221>.
- 6 28. J. Tao, A. Mu, S. Geng, H. Xiao, L. Zhang, Q. Huang, *J. Solid State Electrochem.*
7 2021, **25**, 1959-1974. doi: 10.1007/s10008-021-04984-0.
- 8 29. X. Liu, Y. Tong, Y. Wu, J. Zheng, Y. Sun, L. Niu, H. Li, *Chem. Eng. J.*, 2022, **431**,
9 133986. <https://doi.org/10.1016/j.cej.2021.133986>.
- 10 30. A. Testoni, *First Mediterranean symposium on persimmon.*, 2022, **51**, 53-70.
11 Options Méditerranéennes: Série A.
12 <http://om.ciheam.org/article.php?IDPDF=2600062>
- 13 31. C.G. Park, K.C. Lee, D.W. Lee, H.Y. Choo, P.J. Albert, *J. Chem. Eco.*, 2024, **30**,
14 2269-2283. <https://doi.org/10.1023/B:JOEC.0000048788.35693.23>.
- 15 32. M.S. Butt, M.T. Sultan, M. Aziz, A. Naz, W. Ahmed, N. Kumar, M. Imran, *EXCLI
16 Journal*, 2015, **14**, 542-561. <http://dx.doi.org/10.17179/excli2015-159>.
- 17 33. P. Pérez-Martínez, J.M. Galvan-Miyoshi, J. Ortiz-López, *J. Mater. Sci.*, 2016, **51**,
18 10782–10792. <https://doi.org/10.1007/s10853-016-0290-0>.
- 19 34. L. Stobinski, B. Lesiak, A. Malolepszy, *J Electron Spectrosc Relat Phenom.* 2014,
20 **195**, 145-154. <https://doi.org/10.1016/j.elspec.2014.07.003>.
- 21 35. A.C. Ferrari, *Solid State Commun.*, 2007, **143**, 47-
22 57. <https://doi.org/10.1016/j.ssc.2007.03.052>.
- 23 36. S. Jaworski, M. Wierzbicki, E. Sawosz, A. Jung, G. Gielerak, J. Biernat, H.
24 Jaremek, W. Łojkowski, B. Woźniak, J. Wojnarowicz, L. Stobiński, *Nanoscale Res.
25 Lett.*, 2018, **13**, 1-17 <http://dx.doi.org/10.1186/s11671-018-2533-2>.
- 26 37. M. Athanasiou, S.N. Yannopoulos, T. Ioannides, *Chem., Eng., J.*, 2022, 446,
27 p.137191. <https://doi.org/10.1016/j.cej.2022.137191>.
- 28 38. N.M.S. Hidayah, W.W., Liu, C.W., Lai, N.Z. Noriman, C.S., Khe, U. Hashim, H.C.
29 Lee, *AIP Publishing*, 2017, **1892**. <http://dx.doi.org/10.1063/1.5005764>.
- 30 39. G. Pavoski, T. Maraschin, F. Fim, N. Balzaretto, G. Galland, C. Moura, N. Basso,
31 *Mater. Res.*, 2017, **20**. <https://doi.org/10.1590/1980-5373-MR-2015-0528>.
- 32 40. S.K. Sahoo, A. Mallik, *Nano*, 2015, **10**, 1550019.
33 <https://doi.org/10.1142/S1793292015500198>.



- 1 41. J. Aladekomo, R. Bragg, *Carbon*, 1990, **28**, 897-906. View Article Online
DOI: 10.1039/D6TA01141A
2 [https://doi.org/10.1016/0008-6223\(90\)90338-Y](https://doi.org/10.1016/0008-6223(90)90338-Y).
- 3 42. E. Aliyari, M. Alvand, F. Shemirani, *RSC Adv.*, 2016, **6**, 64193-64202.
4 <https://doi.org/10.1039/C6RA04163A>.
- 5 43. D. Li, M. B. Muller, S. Gilje, R. B. Kaner and G. G. Wallace, *Nat. Nano.* 2008, **3**,
6 101-105. <https://doi.org/10.1038/nnano.2007.451>.
- 7 44. S. Nasir, M.Z. Hussein, N.A. Yusof, and Z. Zainal, *Nanomaterials*, 2017, **7**, p.182.
8 <https://doi.org/10.3390/nano7070182>
- 9 45. A. Sanei, K. Dashtian, J.Y. Seyf, F. Seidi, E. Kolvari, *J. Environ. Management*,
10 2023, 332, p.117377. <https://doi.org/10.1016/j.jenvman.2023.117377>.
- 11 46. Li, Xiao-Rong, Jing Liu, Fen-Ying Kong, Xin-Chun Liu, Jing-Juan Xu, and Hong-
12 Yuan Chen, *Electrochem. Commun.*, 2012, **20**, 109-112.
13 <https://doi.org/10.1016/j.elecom.2012.04.014>.
- 14 47. M. Sevilla, and R. Mokaya, *Energy & Environmental Science*, 2014, **7**(4),
15 pp.1250-1280.
- 16 48. G. Wang, L. Zhang, and J. Zhang, *Chemical society reviews*, 2012, **41**(2), pp.797-
17 828.
- 18 49. E. Huarote-Garcia, A.A. Cardenas-Riojas, I.E. Monje, E.O. López, O.M. Arias-
19 Pinedo, G.A. Planes, and A.M. Baena-Moncada, *ACS Environmental Au*, 2024,
20 **4**(2), pp.80-88.
- 21 50. E. Zhou, J. Xi, Y. Liu, Z. Xu, Y. Guo, L. Peng, W. Gao, J. Ying, Z. Chen, C.
22 Gao, *Nanoscale*, 2017, **9**(47), pp.18613-18618.
- 23 51. N. Sumathi, A.C. Dhanemozhi, D. Thangaraju, S.A. Adewinbi, K. Mohanraj, R.
24 Marnadu, M., Shkir, *Surfaces and Interfaces*, 2021, **26**, p.101408.
- 25 52. *QuantumATK*, Synopsys *QuantumWise A/S*, accessed on Jan. 15, 2024. [Online].
26 Available: <https://www.synopsys.com/silicon/quantumatk.html>.
- 27 53. C. Tewari, B. SanthiBhushan, A. Srivastava, N.G. Sahoo, *Sustain. Chem.*
28 *Pharm.*, 2021, **21**, 100436. <https://doi.org/10.1016/j.scp.2021.100436>.
- 29 54. *MATLAB*, *The MathWorks Inc.*, accessed on Jan 15, 2024. [Online]. Available:
30 www.mathworks.com.
- 31 55. A. Srivastava, and B. SanthiBhushan, *Appl Nanosci.*, 2018, **8**, 637-644.
32 <https://doi.org/10.1007/s13204-018-0643-x>.
- 33 56. B. SanthiBhushan, and A. Srivastava, In *AIP Conference Proceedings*, 2018, **1953**,
34 no. 1. *AIP Publishing*. <https://doi.org/10.1063/1.5033300>.



- 1 57. L. A. Ponomarenko, R. Yang, R. V. Gorbachev, P. Blake, A. S. Mayorov, K. S. View Article Online
2 Novoselov, M. I. Katsnelson, and A. K. Geim, *Phys. Rev. Lett.*, 2010, **105**, 136801. DOI: 10.1039/D6TA01141A
3 <https://doi.org/10.1103/PhysRevLett.105.136801>.

4



Data Availability Statement

The datasets generated during and/or analysed during the current study are available from the corresponding author on reasonable request. All other supporting data are included within the article and its supplementary information.

